

# Magnetic Skyrmions in FePt Square-Based Nanoparticles Around Room-Temperature

Christos Tyrpenou<sup>1</sup>, Vasileios D. Stavrou<sup>1</sup>, and Leonidas N. Gergidis\*<sup>1</sup>

<sup>1</sup>Department of Materials Science and Engineering, University of Ioannina, 45110 Ioannina, Greece

December 21, 2024

## Abstract

Magnetic skyrmions formed around room-temperature in square-based parallelepiped magnetic nanoparticles with perpendicular magnetocrystalline anisotropy similar to that of partially chemically ordered FePt were studied during the magnetization reversal using micromagnetic simulations. Finite Differences (FD) discretizations were used for the solution of the Landau-Lifshitz-Gilbert equation. Magnetic configurations exhibiting Néel chiral stripe and Néel skyrmionic formations were detected. The magnetic skyrmions can be created in different systems generated by the variation of external field, side length and width of the squared-based parallelepiped magnetic nanoparticles. Micromagnetic configurations revealed a variety of states which include skyrmionic textures with one distinct skyrmion formed and being stable for a range of external fields around room-temperature. The size of the formed Néel skyrmion is calculated as a function of the external field, temperature, magnetocrystalline anisotropy and nanoparticle's geometrical characteristic lengths which can be adjusted to produce Néel type skyrmions on demand having diameters down to 12 nm. The micromagnetic simulations revealed that stable skyrmions at the temperature range 270K-330K can be created for FePt magnetic nanoparticle systems lacking of chiral interactions such as Dzyaloshinsky-Moriya, providing new perspectives in the new magnetic writing era.

## 1 Introduction

Magnetic skyrmions are considered by many researchers as dynamic candidates for next generation high density efficient information encoding providing enhanced capabilities in magnetic writing and storage [12, 25, 36, 6, 40]. Their small size and the low current density needed for their manipulation and control [7] pave the way for potential engineering applications. Over the last decade magnetic skyrmions have been under intense theoretical, computational and experimental investigation [28, 16, 4, 20, 41, 26, 23]. It is

of significant importance to understand how the confined nature of geometry can affect skyrmion creation-stabilization and consequently the size and energetics of the skyrmionic states.

Recently, Fert and his collaborators [18] combined concomitant magnetic force microscopy and Hall resistivity measurements to demonstrate the electrical detection of sub-100 nm skyrmions in a multilayered thin film at room-temperature. Additionally, Legrand et al. [13] showed that room temperature antiferromagnetic skyrmions can be stabilized in synthetic antiferromagnets (SAFs), in which perpendicular magnetic anisotropy, antiferromagnetic coupling and chiral order can be adjusted concurrently. In up to date reports room-temperature magnetic skyrmions in ultrathin magnetic multilayer structures of Co/Pd [24], Pt/Co/MgO [1] and Co/Ni [10] were reported. Brãndao et al. [2] reported on the evidence of skyrmions in unpatterned symmetric Pd/Co/Pd multilayers at room temperature without prior application of neither electric current nor magnetic field. Husain et al. [11] observed stable skyrmions in unpatterned Ta/Co<sub>2</sub>FeAl(CFA)/MgO thin film heterostructures at room temperature in remnant state employing magnetic force microscopy showing that these skyrmions consisting of ultrathin ferromagnetic CFA Heusler alloy result from strong interfacial Dzyaloshinskii-Moriya interaction (i-DMI). Ma et al. [17] employed atomistic stochastic Landau-Lifshitz-Gilbert simulations to investigate skyrmions in amorphous ferrimagnetic GdCo revealing that a significant reduction in DMI below that of Pt is sufficient to stabilize ultrasmall skyrmions even in films as thick as 15 nm.

In the present simulation work, the formation of magnetic skyrmions around room-temperature in the external field range used for the magnetization reversal in a single FePt nanoparticle having parallelepiped geometry of square base is studied. The current research effort was inspired-initiated by the variety of skyrmionic magnetic textures detected in FePt triangular and reuleaux prismatic nanoparticles encapsulating multiple skyrmions at 0 K using Finite Elements micromagnetics simulations [30, 9, 31]. It was shown that for magnetocrystalline anisotropy (MCA) values between  $Ku = 200 - 500 \text{ kJ/m}^3$  three distinct skyrmions

\*lgergidi@uoi.gr; lgergidis@gmail.com

are formed and persist for a range of external fields along with rich magnetic structures in the bulk of the FePt nanoparticle similar to those observed in DMI stabilized systems [38]. Néel type skyrmionic textures were detected on the Reuleaux geometry's bases co-existing with Bloch-type textures in the bulk of the FePt nanoelement. It was also shown that the size of skyrmions depends linearly on the field value  $B_{ext}$  and that the slope of the linear curve can be controlled by MCA value [31].

Single layered square-based FePt nanoparticles in the absence of chiral interactions like Dzyaloshinsky-Moriya (DM) or its interfacial analogue (iDM) (present in multi-layered hetero-structures with spin-orbit coupling) are investigated. Skyrmionic textures and formations are explored along with the underlying physical mechanisms for temperatures around 300 K and for different geometrical characteristics of the nanoparticle.

## 2 Micromagnetic modeling

The Landau-Lifshitz-Gilbert (LLG) equation governs the rate of change of the dynamical magnetization field  $\mathbf{M}$  and is given by the relation

$$\frac{d\mathbf{M}}{dt} = \frac{\gamma}{1 + \alpha^2} (\mathbf{M} \times \mathbf{B}_{eff}) - \frac{\alpha\gamma}{(1 + \alpha^2)|\mathbf{M}|} \mathbf{M} \times (\mathbf{M} \times \mathbf{B}_{eff}). \quad (1)$$

The quantity  $\alpha > 0$  is a phenomenological dimensionless damping constant that depends on the material and  $\gamma$  is the electron gyromagnetic ratio. The effective field that governs the dynamical behavior of the system has contributions from various effects that are of very different nature and can be expressed as  $\mathbf{B}_{eff} = \mathbf{B}_{ext} + \mathbf{B}_{exch} + \mathbf{B}_{anis} + \mathbf{B}_{demag} + \mathbf{B}_{thermal}$ . Respectively, these field contributions are the external field  $\mathbf{B}_{ext}$ , the exchange field  $\mathbf{B}_{exch}$ , the anisotropy field  $\mathbf{B}_{anis}$ , the demagnetizing field  $\mathbf{B}_{demag}$  and the thermal field  $\mathbf{B}_{thermal}$ .

In particular, the thermal field  $\mathbf{B}_{thermal}$  which incorporates implicitly the temperature can be expressed by  $\mathbf{B}_{thermal}(t) = \mathbf{n}(t) \sqrt{\frac{2\mu_0\alpha k_B T}{B_{sat}\gamma_{LL}\Delta V\Delta t}}$  according to Brown [3]. In thermal field expression  $\alpha$  is the aforementioned damping constant,  $k_B$  is the Boltzmann constant,  $T$  is the temperature (throughout manuscript slightly slanted  $T$  is used for temperature),  $B_{sat}$  the saturation magnetization expressed in Tesla (T) and  $\gamma$  is the gyromagnetic ratio in units of 1/(T s),  $\Delta V$  the cell volume,  $\Delta t$  the time step and  $\mathbf{n}$  a random vector generated from a standard normal distribution whose value is changed every time step.

For the solution of the LLG equation micromagnetic Finite Differences (FD) calculations have been conducted using Mumax3 Finite Differences software [33, 14]. The dimensionless damping constant  $\alpha$  was set to 1 in order to achieve fast damping and reach convergence quickly as we are interested in static magnetization configurations. The time step used for the integration of the LLG equation was equal to  $\Delta t = 1\text{fs}$ .

The square-based nanoparticle having side length  $a = 150\text{ nm}$  and width  $w = 36\text{ nm}$  will be considered as the reference nanoparticle and will be used for the multi-parametric investigation conducted in the present work. It is chosen since it encapsulates the most stable skyrmion with respect to the magnetic field range and skyrmion type as it will be made clear in the sequel. The particular width value  $w = 36\text{ nm}$  is selected following previous studies [30, 9, 31] which focus on FePt triangular and reuleaux prismatic nanoelements. In addition, the 36 nm thickness of nanoparticle matches that reported in [19]. For the objectives of the multi-parametric study additional magnetic samples-nanoparticles with parallelepiped geometry of square base with varying side length  $a$  from 40 to 180 nm and  $w$  ranging from 6 to 36 nm were also used. The following frame of reference axes assignment convention was used:  $x, y$  along the square's edges, and  $z$  perpendicular to the nanoparticle's square base. The mesh used for the discrete representation of the rectangular parallelepiped nanoelement under study was a regular 3D mesh with characteristic discretization lengths  $\Delta x = \Delta y = 2\text{ nm}$ ,  $\Delta z = 1\text{ nm}$  in  $x, y, z$ -directions respectively. The lengths  $\Delta x, \Delta y, \Delta z$  used for the discretization of the rectangular domain under investigation were lower than the exchange length  $l_{ex} = \sqrt{\frac{2A}{\mu_0 M_s^2}} \approx 3.5\text{ nm}$  for the FePt magnetic material.

The material parameters were chosen similar to the typical bulk FePt parameters with a saturation polarization of  $\mu_0 M_s = 1.43\text{ T}$  ( $M_s = 1.138\text{ MA/m}$ ), and an exchange constant  $A_{exch} = 11\text{ pJ/m}$  which has been found to be independent of the degree of ordering [21]. The magnetocrystalline anisotropy was oriented along  $z$ -axis. The magnetocrystalline anisotropy (MCA) constant was set to  $K_u = 250\text{ kJ/m}^3$  following [9, 31] where interesting skyrmionic textures at the specific magnetocrystalline anisotropy value were reported in triangular and Reuleaux based FePt nanoelements, respectively.

The Finite Differences (FD) micromagnetic simulations were conducted on Nvidia GTX 1080 GPU. The magnetization curves for every production run were investigated by applying external magnetic fields  $B_{ext}$  with fixed orientation running parallel to  $z$ -direction (the normal to the nanoparticle's square base). The range values of  $B_{ext}$  were +1T (maximum) and -1T (minimum) having an external magnetic field step of  $\delta B_{ext} = 0.01\text{ T}$  for the actual magnetic reversal process.

## 3 Results

### 3.1 Skyrmion formation and stabilization for the reference nanoparticle

Skyrmion formation and stabilization as a function of the external field, the geometric characteristics of the nanoparticle and of the temperature can be quantitatively characterized by the calculation of the topological invariant  $S$ , widely known as skyrmion or winding

number [29, 16, 22]. The skyrmion number  $S$  is computed using the relation  $S = \frac{1}{4\pi} \int_A \mathbf{m} \cdot (\frac{\partial \mathbf{m}}{\partial x} \times \frac{\partial \mathbf{m}}{\partial y}) dA$ . The quantity  $\mathbf{m}$  is the unit vector of the local magnetization defined as  $\mathbf{m} = \mathbf{M}/M_s$  with  $\mathbf{M}$  being the magnetization and  $M_s$  the saturation magnetization. Magnetization  $\mathbf{M}$  is provided by the FD numerical solution of the LLG equation. The skyrmion number  $S$  is a physical and topological quantity that measures how many times  $\mathbf{m}$  wraps the unit sphere [16, 35, 8]. Surface  $A$  is the surface domain of integration and corresponds to the square base of the FePt nanoparticles under investigation.

The skyrmion number  $S$  has been computed during the magnetization reversal process as a function of  $B_{ext}$  and is shown in **Fig. 1** for the reference nanoparticle at  $T = 300\text{K}$  and for  $Ku = 250\text{kJ/m}^3$ . The magnetization reversal process is closely followed by the external field step of  $\delta B_{ext} = 0.01\text{T}$ .

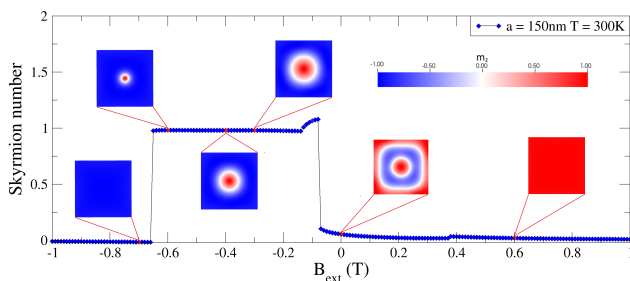


Figure 1: Skyrmion number  $S$  as a function of  $B_{ext}$  for the reference nanoparticle at 300K. The pseudo color which is shown in the depicted micromagnetic configurations refers to the  $z$ -component of magnetization ( $m_z$ ).

As the external field decreases the magnetic system departs from saturation through a series of trivial configurations followed by a gradual increase of the skyrmion number. Skyrmion number values  $S = 0.03 - 0.1$  start to appear for  $B_{ext} = (+0.1\text{T}) - (-0.07\text{T})$ . Infinitesimal decrease of the magnetic field below  $B_{ext} = -0.07\text{T}$  triggers a jump-like discontinuity on skyrmion number. The value of  $S$  abruptly increases from  $S = 0.1$  to  $S = 1.1$ . Further decrease of the external field does not affect the skyrmion number which develops an extended plateau region with  $S = 1$  for external field values down to  $B_{ext} = -0.65\text{T}$ . For magnetic field value below  $B_{ext} = -0.65\text{T}$  a new abrupt jump-like reduction this time of skyrmion number  $S$  signals the annihilation of the formed skyrmion and the finalization of the magnetization reversal process.

The numerical solution of the LLG equation allows the direct representation and inspection of the micromagnetic configurations. These configurations are also shown in **Fig. 1** for representative values of the external field. It should be noted that the pseudo color used for the micromagnetic configurations refers to  $z$ -component of magnetization ( $m_z$ ). At the initial states of the reversal process the magnetization vectors are aligned parallel to the external field (red colored square in **Fig. 1**). Around the external mag-

netic field of 0 T magnetic structures are formed having a skyrmionium-type. A magnetic skyrmionium is a non-topological soliton which has a doughnut-like out of plane spin texture in magnetic nanoparticles and thin films. It can be viewed as a coalition of two magnetic skyrmions with opposite skyrmion numbers giving a zero total skyrmion number  $S_{skyrmionium} = 0$  [39, 37]. The skyrmionium ( $S = 0.1$ ) considered as a distinct skyrmionic state with particular characteristics [39] heralds the abrupt transition to a clear skyrmionic state ( $S = 1$ ). The formed skyrmion which has a perfect circular shape is a Néel-type skyrmion and as mentioned earlier remains stable for an external field range. In the one skyrmion plateau region as the field value decreases from  $B_{ext} = -0.08\text{T}$  to  $B_{ext} = -0.65\text{T}$  the actual diameter of the skyrmion also decreases as it can be seen from the representative micromagnetic configurations exposed in **Fig. 1**. The magnetization reversal process is complete when all magnetization vectors are aligned parallel to ( $-z$ ) direction (blue colored square in **Fig. 1**).

### 3.2 Skyrmion dependence on nanoparticles's width

For nanoparticles having  $a = 150\text{nm}$  individual micromagnetic simulations have been conducted at different  $w$  values in order to investigate the effect of the nanoparticle's width on the actual skyrmion formation during the magnetization reversal process at the temperature of 300K. The skyrmion number  $S$

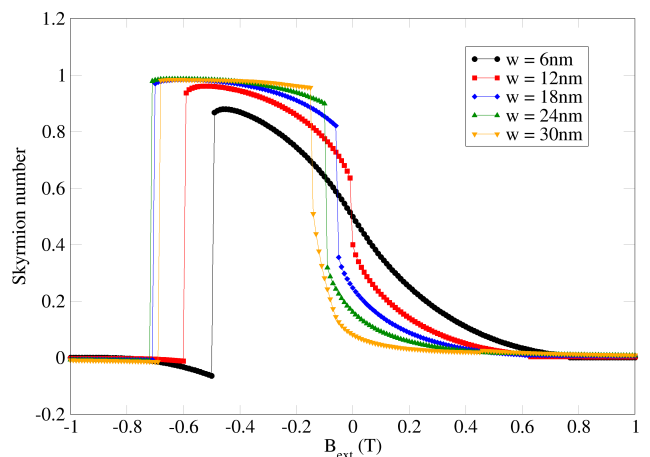


Figure 2: Skyrmion number  $S$  as a function of  $B_{ext}$  for side value  $a = 150\text{nm}$  at 300K for geometries having different widths  $w = 6, 12, 18, 24, 30\text{nm}$ .

as a function of  $B_{ext}$  is shown for width values  $w = 6, 12, 18, 24, 30\text{nm}$  in **Fig. 2**. Skyrmion can be produced in substantial ranges even for widths down to 6 nm. The present FD micromagnetic simulations reveal that the 6 nm width for  $a = 150\text{nm}$  nanoparticle is critical for the creation of skyrmions. Widths having values below 6 nm cannot produce complete skyrmions. The line shape for the nanoparticle with  $w = 6\text{nm}$  substantially deviates from the nanoparticles with different widths showing a smoother increase of

the skyrmion number as a function of the external magnetic field during the skyrmion's creation process. The nanoparticles with  $w = 12 - 36$  nm expose a discontinuous jump-like character for external fields around 0 T. The higher the width the higher the jump-like discontinuity. For all widths the annihilation of skyrmion occurring in different field values is an abrupt process where skyrmion number goes from  $S = 1$  to  $S = 0$  with no intermediate transition magnetic states.

### 3.3 Skyrmion dependence on MCA

For the reference nanoparticle ( $a = 150$  nm,  $w = 36$  nm) simulations have been conducted with varying MCA values  $Ku = 150 - 450$  kJ/m<sup>3</sup> while its orientation is set parallel to external field and  $z$ -direction. It is interesting the fact that MCA mainly affects the magnetic field range of stabilization of the skyrmion formed and not the skyrmionic state of  $S = +1$ . Two external fields during the creation ( $B_{start}$ ) and the annihilation ( $B_{end}$ ) of skyrmion were recorded and presented in **Fig. 3**. The  $B_{start}$  values of the magnetic field show small differentiations around -0.1T having an undulating shape with the gradual increase of the MCA from  $Ku = 150$  kJ/m<sup>3</sup> to  $Ku = 450$  kJ/m<sup>3</sup>. The skyrmion annihilation field value of  $B_{end}$  exposes a clear gradual increase from -0.7T to -0.5T as the MCA value increases. The external magnetic field skyrmion's stabilization range  $|B_{end} - B_{start}|$  is also monitored in **Fig. 3** exposing rather monotonic decrease as MCA value increases interrupted for the values of  $Ku = 250, 450$  kJ/m<sup>3</sup>.

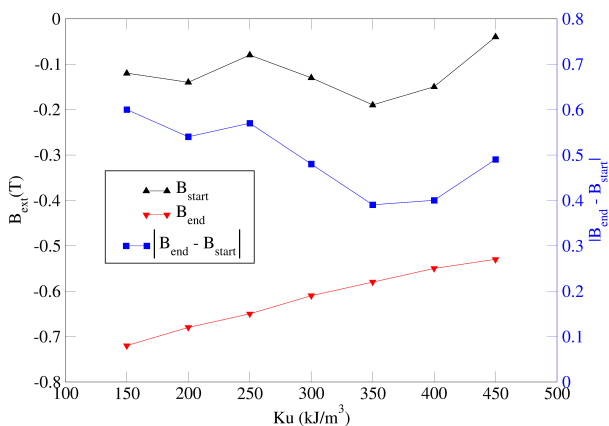


Figure 3: External fields relative to the formation ( $B_{start}$ ) and annihilation ( $B_{end}$ ) as a function of MCA value ( $Ku = 150 - 450$  kJ/m<sup>3</sup>) for the reference nanoparticle at 300K.

### 3.4 Skyrmion dependence on temperature

The effect of the temperature which is introduced implicitly through the effective thermal field has been investigated for the reference nanoparticle. Individual simulations at temperature range  $300\text{K} \pm 30$  K have been conducted. Since the crucial result in terms of

the technological applications is the skyrmion formation and its stability in a range of fields around room-temperature two skyrmion number susceptibilities were computed for the particular temperature range. This computation will allow the quantitative description of the temperature effect on skyrmions. The susceptibilities  $\chi_S^{(1,2)}$  are similar to those proposed in [27]. Susceptibility  $\chi_S^{(1)}$  is defined as

$$\chi_S^{(1)} = \frac{1}{T} (\langle S^2 \rangle - \langle S \rangle^2) \quad (2)$$

while the relative susceptibility with respect to  $\langle S \rangle$  is given by

$$\chi_S^{(2)} = \frac{\chi_S^{(1)}}{\langle S \rangle}. \quad (3)$$

The average value of the skyrmion number ( $\langle S \rangle$ ) is calculated by

$$\langle S \rangle = \frac{1}{|B_{end} - B_{start}|} \int_{B_{start}}^{B_{end}} S(B_{ext}) dB_{ext} \quad (4)$$

where  $B_{start}$ ,  $B_{end}$  represent the external fields during the creation and annihilation of skyrmion respectively. From **Fig. 4** is evident that temperatures 30 K below or above the temperature of 300 K do not affect the skyrmion formation and stabilization. This is a significant manifestation for the skyrmion creation and stabilization at room-temperature in FePt nanoparticles strengthening our perspective for their potential information storage applications.

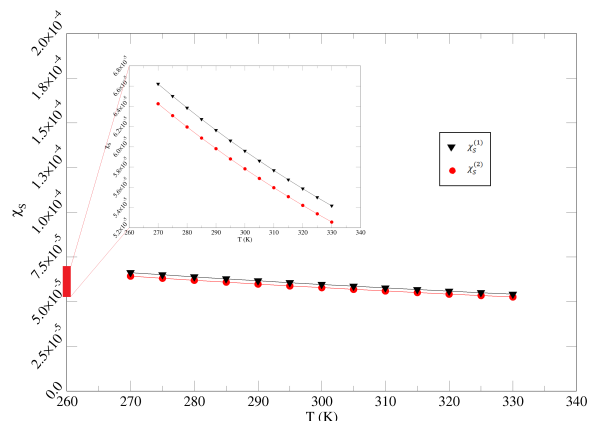


Figure 4: Skyrmion susceptibility  $\chi_S$  calculated in a range of temperatures from 270 to 330K. The inset graph represents a magnification of the actual  $\chi_S$  region spotted with the red highlighted part of the vertical axis.

### 3.5 Skyrmionic states-Skyrmion dependence on the square's base side length

From the results presented and the conclusions drawn so far it is clear that skyrmionic textures can be created and stabilized by adjusting the width, the MCA value and the temperature of the magnetic system. The skyrmion number  $S$  has been computed

during the magnetization reversal of FePt nanoparticles with variable size. The **Fig. 5** depicts for the temperature of 300K,  $Ku = 250\text{kJ/m}^3$  and  $w = 36$  nm a skyrmionic state diagram constructed by the different values of external field  $B_{ext}$  and of the square side length  $a$ . The topological invariant  $S$  reported along with the actual magnetic configurations can provide valuable qualitative information towards the detection and characterization of skyrmionic states. It is very interesting the fact that a wide variety of micromagnetic skyrmionic states emerges for the square-based FePt nanoparticles. The most commonly detected micromagnetic states are presented along with the respective skyrmion number  $S$  in **Fig. 6** and can be assigned to the following categories:

- a, b. Uniform states:** States where the magnetization is uniform and the actual magnetization vectors point all upwards (red color) or all downwards (blue color) [5, 23].
- c. Helical state:** A variety of rotational spin textures [23].
- d. Skyrmionium:** A magnetic skyrmionium is a non-topological soliton of a doughnut shape [39, 37].
- e. Skyrmion with  $S = -1$ :** A counterclockwise circulation (positive circulation), the central spins of the skyrmion point inwards (negative polarity) [22, 9].
- f. Néel chiral stripe or Néel-Stripe:** A Néel-stripe formations resemble two skyrmions which are united having an elongated shape [15].
- g. Skyrmion with  $S = 1$  - State where one skyrmion is formed [22, 9].**
- h. X states -** Micromagnetic states with  $S \approx 0$  having an X-shape serving as short-lived rarely detected transition states.

Nanoparticles with side length  $a = 40, 50, 60\text{nm}$  are not capable of hosting skyrmionic entities irrespective of the applied external field as can be seen in **Fig. 5**. As the side length increases ( $a = 70, 80, 90\text{nm}$ ) helical states appear for  $B_{ext} = (-0.1\text{T}) - (+0.1\text{T})$ . Skyrmions start to appear for square bases with  $a \geq 100\text{nm}$  and for  $B_{ext} > 0$  values. It is interesting the fact that nanoparticle with  $a = 100$  nm has skyrmion ignition field value at  $+0.1\text{T}$  while nanoparticles with  $a = 110 - 140$  nm at  $+0.2\text{T}$ . The skyrmion number values is in  $[-0.98, -0.92]$  interval. Skyrmionic states for the  $a = 100, 110$  nm nanoparticles although similar to their initial generation stages with those of  $a \geq 120\text{nm}$  nanoparticles, expose some substantial differences as the external field decreases and passes to negative values. For the  $a = 100, 110$  nm nanoparticles which host one skyrmion ( $S \approx -1$ ) for field values down to  $0\text{T}$ , the further reduction of the external field drives the final annihilation of the skyrmion.

Magnetic nanoparticles that promote the creation and stabilization of skyrmions in a considerable range of external fields are the nanoparticles with square side length in the  $a = 120 - 150$  nm range. Interestingly, for  $a = 120$  nm one skyrmion with  $S = -1$  in the field range  $[-0.1\text{T}, 0.2\text{T}]$  can be created and transformed to skyrmion with  $S = +1$  which immediately

gain its stability in the range of  $[-0.5\text{T}, -0.2\text{T}]$ . For  $a = 130 - 140$  nm side length skyrmions with  $S = +1$  can be created from skyrmions with  $S = -1$  through intermediate states having X-shapes. The most stable skyrmion with respect to the field range  $([-0.6\text{T}, -0.1\text{T}])$  and type (Néel) is observed for  $a = 150$  nm. This is the reason why the particular magnetic nanoparticle is used as the reference system for the multi-parametric investigations adopted.

The micromagnetic simulations conducted for bigger nanoparticles with side lengths beyond  $150$  nm ( $a = 160, 170, 180$  nm) allow the creation of new skyrmionic states such as Néel chiral stripes. Néel stripe textures appear for the particular external field value of  $B_{ext} = -0.2\text{T}$  for  $a = 160, 170$  nm. For the biggest nanoparticle having  $a = 180\text{nm}$  the Néel chiral stripe is apparent for  $B_{ext} = -0.2\text{T}$  and  $-0.3\text{T}$ . Néel chiral stripes can not be stabilized in a wide range of magnetic fields. Through a closer inspection of **Fig. 5** one can draw the conclusion that Néel chiral stripes serve as intermediate transition states from the incomplete skyrmions-skyrmionic textures having  $S = 0.1 - 0.8$  to the final stable circular Néel-type skyrmions.

### 3.6 Nanoparticle's internal magnetic structure

Finite Difference micromagnetic simulations can provide rich and detailed information about the magnetization behavior on the surface and in the bulk of nanoparticle. The detected skyrmions on the surface are inevitably related to the magnetization formations on the internal domain of the nanoparticle. The existence of magnetic structure in the internal domain of the magnetic nanoparticle can be revealed by monitoring the magnetization vectors  $\mathbf{M}$  for grid points located at different  $z$ -levels ( $xy$ -cross section) and for  $yz, xz$  - cross sections. These cross sections were chosen for micromagnetic systems hosting one skyrmion of different type (Néel, Néel chiral stripe) in order to describe the qualitative characteristics of the actual skyrmionic texture. Néel skyrmion is shown in **Fig. 7** for the reference geometry and for  $B_{ext} = -0.3$  T. Néel chiral stripe skyrmion with  $180$  nm side length and  $36$  nm width is shown in **Fig. 8** for  $B_{ext} = -0.2$  T. Both were depicted for MCA value  $Ku = 250\text{kJ/m}^3$ .

At first glance the presence of magnetic structure is evident for Néel (**Fig. 7**) and Néel chiral stripe skyrmions (**Fig. 8**) in all the cross sections visualized. In particular,  $xy$ -cross sections at  $z = 0, 9, 18, 27, 36$  nm reveal skyrmionic configurations appearing in each square  $z$ -level and are presented in **Fig. 7**. Interesting is the fact that micromagnetic configurations in the non-surface  $z$ -values expose different magnetic characteristics with respect to skyrmions observed on the square bases of the FePt nanoparticle. On the top or bottom surface Néel and Néel chiral stripe skyrmions are formed while in the proximity of central bulk region magnetization vectors deviate ( $z = 9, 27$  nm of **Fig. 7**) from the Néel skyrmion pattern adopting a more Bloch-type skyrmionic magnetic

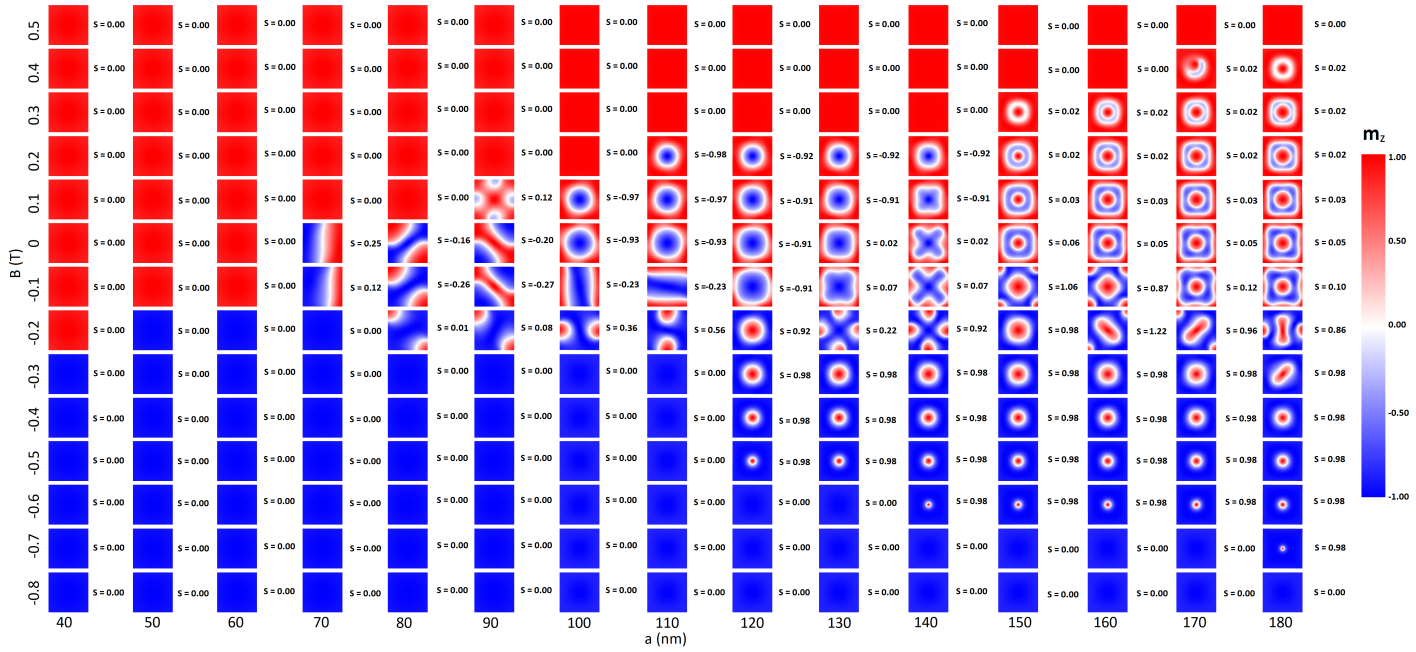


Figure 5: Micromagnetic states revealed at 300K for the FePt nanoparticle. The color bar refers to the  $z$ -component of magnetization ( $m_z$ ).

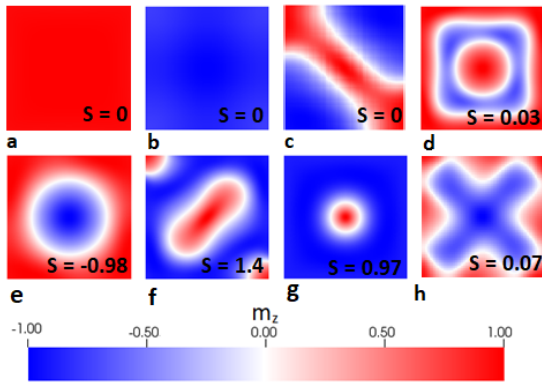


Figure 6: Different states detected for the square base nanoelement. The states are: (a), (b) uniform, (c) helical, (d) skyrmionium, (e) skyrmion with  $S = -1$ , (f) Néel chiral stripe, (g) skyrmion with  $S = +1$ , (h) X-shape

texture at  $z = 18$  nm with vortex type circulating magnetizations. It is worth mentioning that the elongated Néel chiral stripe skyrmion has a perfectly developed magnetization circulation following the exact perimeter of the particular skyrmion exposed in (Fig. 8) also at half width  $z = 18$  nm. The size of the skyrmionic regions at different  $z$ -levels is similar.

Magnetization configurations represented by the magnetization vector on the nodal points at  $z=0$  nm and  $z=36$  nm are different as can be observed in Figs. 7, 8. It should be pointed out that for the two aforementioned  $z$ -levels where the magnetization configurations hosting skyrmions might seem different they are topologically equivalent. This can be justified by the fact that the calculated integrals of the topological invariant  $S$  on the two square base areas are the same.

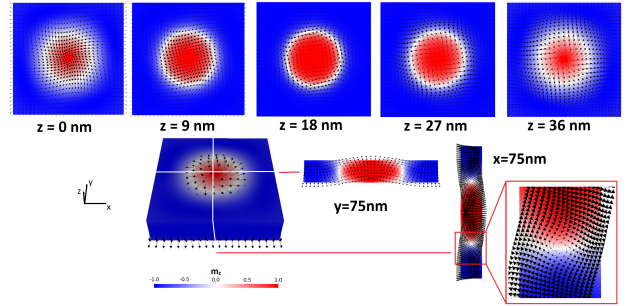


Figure 7: Micromagnetic configurations of a Néel skyrmion at different  $z$ -levels ( $z = 0, 9, 18, 27, 36$  nm) for  $B_{ext} = -0.3T$  and for the reference nanoparticle at 300K. In addition,  $xz$  and  $yz$ -cross sections sliced at  $y = 75, x = 75$  nm respectively are depicted for the square-base parallelepiped geometry of the magnetic nanoparticle. In particular, a magnified domain of the  $yz$ -cross section is also shown. The color bar represents the  $z$ -component of the magnetization ( $m_z$ ).

The present simulation results support the depth dependence of helicity which is an interesting result that has been recently observed experimentally by tomography in systems with bulk skyrmions reported by Zhang et al. [38]. It should be pointed out that although the physics behind skyrmion formation in this system may differ the depth dependence is obviously related to surface effects in both systems. In the present case where skyrmions are created in thin nanoparticles the depth dependence of the demagnetizing field (which has increased  $z$ -component near the surfaces [32]) can force the vortex to acquire a Néel character at the surfaces while maintaining its typical chiral nature at the bulk. The skyrmionic structures observed here depend

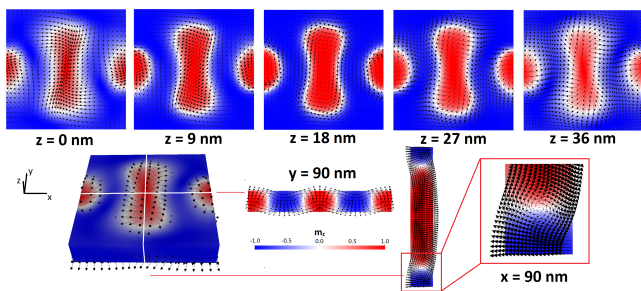


Figure 8: Micromagnetic configurations of a Néel chiral stripe skyrmion at different  $z$ -levels ( $z = 0, 9, 18, 27, 36$  nm) for  $B_{ext} = -0.2$ T and side value of 180nm at 300K. In addition,  $xz$  and  $yz$ -cross sections sliced at  $y = 90, x = 90$ nm respectively are depicted for the square-base parallelepiped geometry of the magnetic nanoparticle. In particular, a magnified domain of the  $yz$ -cross section is also shown. The color bar represents the  $z$ -component of the magnetization ( $m_z$ ).

on the demagnetizing effects which are proportional to the thickness  $w$  (as the easy axis remains in-plane) and vanish for low thickness values ( $< 6$  nm) as it was shown from the presentation of the current simulation results and discussion. Inevitably, the rich skyrmionic textures and physical phenomena related to the depth dependence of helicity are being suppressed as the thickness becomes comparable to the exchange length ( $l_{ex}$ ).

At  $xz$ -cross section (sliced at  $y=75$ nm) which hosts the Néel skyrmion the magnetization vectors develop three distinct regions along the  $x$ -direction as exposed in **Fig. 7** with two clear vortex-like magnetization circulations on the interfaces between the regions. In the regions (blue-shaded) located at the right and left corners of  $xz$ -cross section magnetizations are pointing downwards with the dimensionless magnetization  $z$ -component attaining values  $m_z = -1$ . Moving away from the corners towards the skyrmionic bulk regions the tilting of magnetizations starts producing the aforementioned vortex formations at the interfaces. At the central bulk region the magnetizations start to align parallel to  $z$ -direction pointing upwards ( $m_z = +1$ ). The Néel stripe skyrmionic texture exposes very similar behavior with alternating magnetization orientation between the successive red-blue-central red-blue-red domains as can be seen from the  $xz$ -cross section shown in **Fig. 8**. Vortex like formations are also evident at the interfaces.

The  $yz$ -cross section is also shown for the Néel and Néel stripe skyrmion in **Fig. 7** and **Fig. 8**, respectively. A circulation region is located at the center of the  $yz$ -cross section. Distinct regions hosting parallel magnetizations pointing downwards (blue-shaded region with  $m_z = -1$ ) and upwards (red-shaded region with  $m_z = +1$ ) are evident. Their position follows an alternating fashion blue-red-blue with the interface regions (white region having  $m_z = 0$ ) hosting the center of vortex formations.

### 3.7 Skyrmion's size-diameter

The isolated Néel skyrmions that have been generated on the FePt nanoparticle of square parallelepiped geometries during the reversal process have circular geometry with varying diameter  $d_{sk}$ . Their size can be controlled by the magnitude of external field as reported in the recent literature [34] and shown by Finite Element micromagnetics simulations for FePt nanoparticles having reuleaux geometries at 0 K [31]. The skyrmion's size dependence on the external field and on the square base side length  $a$  is computed and quantified.

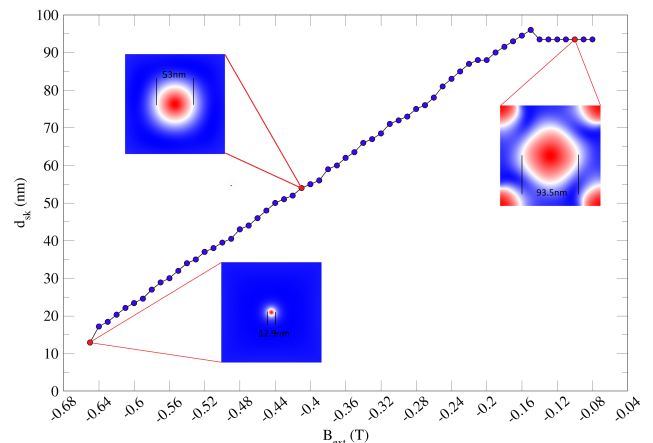


Figure 9: Skyrmion's diameters  $d_{sk}$  at  $T = 300$ K as a function of the applied external field  $B_{ext}$  along with representative micromagnetic configurations for the reference nanoparticle ( $a = 150$  nm  $w = 36$  nm).

In **Fig. 9** the calculated skyrmion diameter  $d_{sk}$  is shown as a function of the external field for values between  $-0.08$ T and  $-0.65$ T. These  $B_{ext}$  values define the range in which the skyrmion number remains constant at value  $S = 1$ . The newly formed skyrmion at  $B_{ext} = -0.08$ T has a diameter around 90 nm. The skyrmion conserves its size for external field values up to  $-0.15$ T. Further decrease of  $B_{ext}$  below  $-0.15$ T triggers a gradual reduction of the skyrmion diameter and consequently of the skyrmion size. The reduction of skyrmion's diameter with respect to  $B_{ext}$  follows the linear relation  $d_{sk} = 162.6B_{ext} + 120.94$ . The external magnetic field plays a dominant role on the actual size of the Néel-skyrmion.

The geometrical characteristics of the parallelepiped nanoparticle with square base are also studied. Néel skyrmion's diameters  $d_{sk}$  at  $T = 300$ K,  $Ku = 250$ kJ/m<sup>3</sup> and for external field value  $B_{ext} = -0.4$ T were calculated as functions of nanoparticle's width ( $w$ ) and square's side length ( $a$ ). **Fig. 10** shows in blue color  $d_{sk}(w)$  with the side length set to  $a = 150$  nm and  $d_{sk}(a)$  having constant width  $w = 36$  nm. The increase of  $w$  is followed by a monotonic increase of  $d_{sk}$  with two apparent regimes. In the first one ranging from  $w = 6$  to 24nm the diameter  $d_{sk}$  increases from 15 to 30 nm. Inside the second regime which extends beyond the threshold value of  $w = 24$ nm the increase

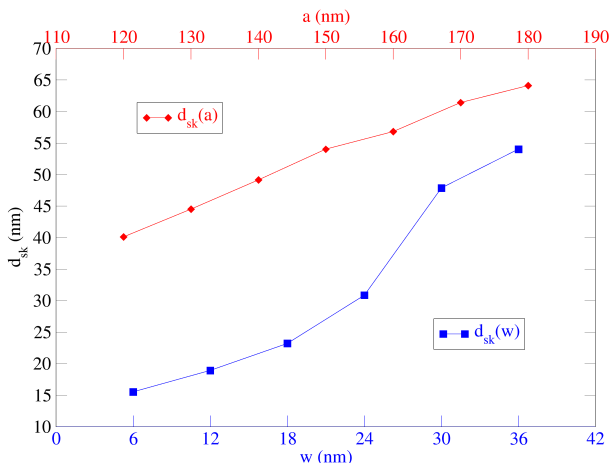


Figure 10: Skyrmion's diameters  $d_{sk}$  at  $T = 300K$ ,  $Ku = 250kJ/m^3$ ,  $B_{ext} = -0.4T$  as a function of nanoparticle's width  $w$  in blue color (side length was set to  $a = 150$  nm) and as a function of the side length  $a$  in red color (width length was set to  $w = 36$  nm).

of  $w$  from 24 to 36 nm causes the abrupt increase of the diameter values from 30 to 55 nm. The square side length  $a$  of the nanoparticle has a linear relation with  $d_{sk}$  as it can be seen in **Fig. 10** (in red color). The increase of the side length causes the increase of  $d_{sk}$  obeying  $d_{sk}(a) = 0.40514a - 7.9014$  nm.

In order to have an additional but coarser comparison for the sizes of skyrmions formed between square parallelepipeds having different side lengths ( $a$ ) the skyrmion's diameter is computed during the last stages of the magnetization reversal. In **Fig. 11** the skyrmion's diameter  $d_{sk}$ , the external field values  $B_{ext}$  just before the annihilation of the skyrmion are shown as a function of the square side  $a$  at  $T = 300K$ . As the side of the square base  $a$  is increased the skyrmion's annihilation field moves to more negative values. The lowest skyrmion's annihilation field is  $-0.7T$  for  $a=180nm$ . The highest value for skyrmion's diameter is  $d_{sk}^{max} = 15.8nm$  and can be achieved with nanoparticle geometry having  $a=180$  nm side length. As the side length  $a$  reduces  $d_{sk}$  also reduces attaining its minimum value close to 12 nm for  $a=140$  nm. Further decrease is followed by a slight diameter increase leading to values around  $d_{sk} \approx 14nm$ .

The skyrmion diameter-size has been calculated at different MCA values for the reference nanoparticle and the results are given in **Fig. 12** for the specific value of  $B_{ext} = -0.4T$ . At first glance two different linear regimes with different values and signs for the slopes exist describing the skyrmion's size dependence on the MCA value. Lower MCA values have a stronger effect on  $d_{sk}$ . In particular, as MCA value gradually increases from 150, to 200 and finally to 250  $kJ/m^3$  the diameter of skyrmion increases attaining the values  $d_{sk} = 37, 40, 54$  nm, respectively. The  $d_{sk} = 54$  nm value is the maximum skyrmion diameter obtained through the variation MCA. Further increase of the MCA to values up to  $Ku = 450kJ/m^3$  causes the diameter of the skyrmion to decrease almost linearly to 47.5 nm.

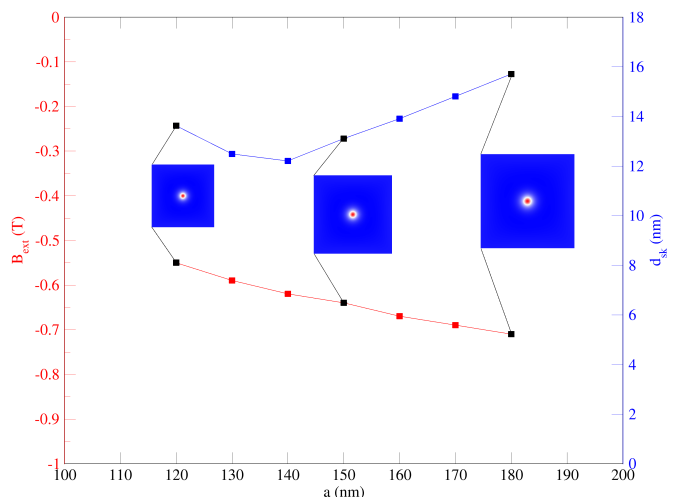


Figure 11: Skyrmion's diameters  $d_{sk}$  (in blue), the external field value  $B_{ext}$  (in red) just before the annihilation of the skyrmion are shown as a function of the square side  $a$  (width length was set to  $w = 36$  nm) along with the representative micromagnetic configurations at  $T = 300K$ .

Finally, the skyrmion diameter for the reference nanoparticle for  $Ku = 250kJ/m^3$  and  $B_{ext} = -0.4$  T has been calculated for different temperatures around 300K as can be seen also in **Fig. 12**. It is clear that the temperature does not affect the size of the created skyrmion even for temperatures 30K above or below the room-temperature.

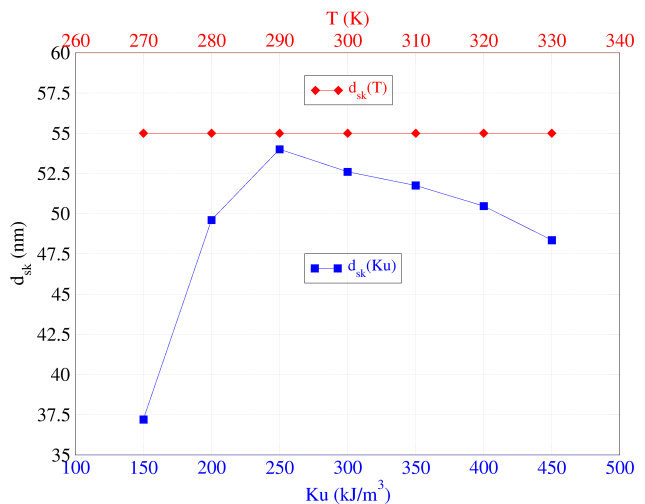


Figure 12: Skyrmion's diameters  $d_{sk}$  for magnetic field value  $B_{ext} = -0.4$  T as a function of temperature  $T$  (red horizontal axis) and of MCA  $Ku$  (blue horizontal axis)) for the reference square-based nanoparticle.

## Conclusions

Finite Differences numerical simulations have been conducted taking into account thermal effects in the form of Brownian term in the effective field involved in LLG equation in order to investigate the forma-

tion of skyrmions at the temperature range of 270K-330K. Magnetic skyrmions have been detected during the magnetization reversal process for FePt square-based parallelepiped nanoparticles having different side lengths and widths with MCA value kept constant at  $Ku=250\text{kJ/m}^3$ . MCA and external field were set normal to nanoparticle's surface in all conducted numerical simulations. Computation of the topological invariant of skyrmion number  $S$  accompanied by the visualization of the actual micromagnetic configurations have provided detailed quantitative and qualitative information relative to skyrmion formation and stabilization. Interesting magnetic structures were revealed for particular external magnetic field value ranges. Néel type skyrmionic textures were detected on the outer surfaces coexisting with Bloch-type textures in the bulk of the FePt square-based parallelepiped nanoelements.

The sizes of Néel skyrmions were computed showing a linear dependence with respect to the external field and of the side length  $a$ . The geometries with side lengths larger than 140 nm can give close to skyrmion's annihilation magnetic fields Néel skyrmions with higher diameters close to 16nm. In conjunction with previous finite element studies at 0K it is clear that magnetic skyrmions can be produced around 300K in a wide range of external fields, even in the absence of chiral interactions such as Dzyaloshinsky-Moriya for FePt nanoparticles.

## Acknowledgments

V. D. Stavrou is supported through the Operational Programme "Human Resources Development, Education and Lifelong Learning" in the context of the project "Strengthening Human Resources Research Potential via Doctorate Research" (MIS-5000432), implemented by the State Scholarships Foundation (IKY) co-financed by Greece and the European Union (European Social Fund-ESF). We would like to thank Mr. Konstantinos Dimakopoulos for his technical support.

## References

- [1] O. Boulle, J. Vogel, H. Yang, S. Pizzini, D. De Souza Chaves, A. Locatelli, T.O. Mendes, A. Sala, L.D. Buda-Prejbeanu, O. Klein, M. Belmeguenai, Y. Roussigne, A. Stashkevich, S. Mourad Cherif, L. Aballe, M. Foerster, M. Chshiev, S. Auffret, I.M. Miron, and G. Gaudin. Room-temperature chiral magnetic skyrmions in ultrathin magnetic nanostructures. *Nature Nanotechnology*, 11(5):449–454, 2016.
- [2] J. Brandao, D.A. Dugato, R.L. Seeger, J.C. Denardin, T.J.A. Mori, and J.C. Cezar. Observation of magnetic skyrmions in unpatterned symmetric multilayers at room temperature and zero magnetic field. *Scientific Reports*, 9(1):4144, 2019.
- [3] William Fuller Brown. Thermal fluctuations of a single-domain particle. *Phys. Rev.*, 130:1677–1686, Jun 1963.
- [4] Felix Büttner, Ivan Lemesch, and Geoffrey S. D. Beach. Theory of isolated magnetic skyrmions: From fundamentals to room temperature applications. *Scientific Reports*, 8:4464, 2018.
- [5] C. P. Chui, Fusheng Ma, and Yan Zhou. Geometrical and physical conditions for skyrmion stability in a nanowire. *AIP Advances*, 5(4):047141, 2015.
- [6] K. Everschor-Sitte, J. Masell, R. M. Reeve, and M. Kläüi. Perspective: Magnetic skyrmions—overview of recent progress in an active research field. *Journal of Applied Physics*, 124(24):240901, 2018.
- [7] Albert Fert, Nicolas Reyren, and Vincent Cros. Magnetic skyrmions: advances in physics and potential applications. *Nature Reviews Materials*, 2(7):17031, 2017.
- [8] T. Fischbacher, M. Franchin, G. Bordignon, and H. Fangohr. Ground state search, hysteretic behaviour, and reversal mechanism of skyrmionic textures in confined helimagnetic nanostructures. *Scientific Reports*, 5:6784, 2015.
- [9] Leonidas N. Gergidis, Vasileios D. Stavrou, Drosos Kourounis, and Ioannis Panagiotopoulos. Micro-magnetic simulations study of skyrmions in magnetic FePt nanoelements. *Journal of Magnetism and Magnetic Materials*, 481:111 – 121, 2019.
- [10] A. Hrabec, M. Sampaio, J. Belmeguenai, I. Gross, R. Weil, S. M. Cherif, A. Stashkevich, V. Jacques, A. Thiaville, and S. Rohart. Current-induced skyrmion generation and dynamics in symmetric bilayers. *Nature Communications*, 8:15765, 2017.
- [11] S. Husain, N. Sisodia, A.K. Chaurasiya, A. Kumar, J.P. Singh, B.S. Yadav, S. Akansel, K.H. Chae, A. Barman, P.K. Muduli, P. Svedlindh, and S. Chaudhary. Observation of skyrmions at room temperature in  $\text{Co}_2\text{FeAl}$  heusler alloy ultrathin film heterostructures. *Scientific Reports*, 9(1):1085, 2019.
- [12] N. S. Kiselev, A. N. Bogdanov, and R. Schafer abd U. K. Robler. Chiral skyrmions in thin magnetic films: new objects for magnetic storage technologies. *Journal of Applied Physics D*, 44:392001, 2011.
- [13] W. Legrand, D. Maccariello, F. Ajejas, S. Collin, A. Vecchiola, K. Bouzehouane, N. Reyren, V. Cros, and A. Fert. Room-temperature stabilization of antiferromagnetic skyrmions in synthetic antiferromagnets. *Nature Materials*, page in press, 2019.

- [14] Jonathan Leliaert, Mykola Dvornik, Jeroen Mulkers, Jonas De Clercq, Milorad V Milosevic, and Bartel Van Waeyenberge. Fast micromagnetic simulations on GPU : recent advances made with mumax3. *Journal of Physics D-Applied Physics*, 51(12):31, 2018.
- [15] Shi-Zeng Lin. Edge instability in a chiral stripe domain under an electric current and skyrmion generation. *Phys. Rev. B*, 94:020402, Jul 2016.
- [16] J. Ping Liu, Zhidong Zhang, and Guoping Zhao. *Skyrmions: Topological Structures, Properties, and Applications*. CRC PRESS, Boca Raton, 2017.
- [17] C.T. Ma, Y. Xie, H. Sheng, A.W. Ghosh, and S.J. Poon. Robust formation of ultrasmall room-temperature Néel skyrmions in amorphous ferrimagnets from atomistic simulations. *Scientific Reports*, 9(1):9964, 2019.
- [18] D. Maccariello, W. Legrand, N. Reyren, K. Garcia, K. Bouzehouane, S Collin, V. Cros, and A. Fert. Electrical detection of single magnetic skyrmions in metallic multilayers at room temperature. *Nature Nanotechnology*, 13:233–237, 2018.
- [19] A. Markou, K. G. Beltsios, L. N. Gergidis, I. Panagiotopoulos, T Bakas, K. Ellinas, A. Tserepi, L. Stoleriu, R. Tanasa, and A. Stancu. Magnetization reversal in triangular L10-FePt nanoislands. *Journal of Magnetism and Magnetic Materials*, 344:224–229, 2013.
- [20] C. Moreau-Luchaire, C. Moutafis, N. Reyren, J. Sampaio, C. A. F. Vaz, N. Van Horne, K. Bouzehouane, K. Garcia, C. Deranlot, P. Warnicke, P. Wohlhüter, J.M. George, M. Weigand, J. Raabe, V. Cros, and A. Fert. Additive interfacial chiral interaction in multilayers for stabilization of small individual skyrmions at room temperature. *Nature Nanotechnology*, 11:444–448, 2016.
- [21] S. Okamoto, N. Kikuchi, O. Kitakami, T. Miyazaki, Y. Shimada, and K. Fukamichi. Chemical-order-dependent magnetic anisotropy and exchange stiffness constant of FePt (001) epitaxial films. *Phys. Rev. B*, 66:024413, 2002.
- [22] Krisztián Palotás. High-resolution combined tunneling electron charge and spin transport theory of Néel and Bloch skyrmions. *Phys. Rev. B*, 98:094409, Sep 2018.
- [23] Ryan A. Pepper, Marijan Beg, David Cortés-Ortuño, Thomas Kluyver, Marc-Antonio Bisotti, Rebecca Carey, Mark Vousden, Maximilian Albert, and Weiwei Wang, Ondrej Hovorka, and Hans Fangohr. Skyrmion states in thin confined polygonal nanostructures. *Journal of Applied Physics*, 123:093903, 2018.
- [24] Shawn D. Pollard, Joseph A. Garlow, Jiawei Yu, Zhen Wang, Yimei Zhu, and Hyunsoo Yang. Observation of stable Néel skyrmions in Co/Pd multilayers with lorentz transmission electron microscopy. *Nature Communications*, 8:14761, 2017.
- [25] N. Romming, C. Hanneken, M. Menzel, J. E. Bickel, B. Wolter, K. von Bergmann, A. Kubetzka, and R. Wiesendanger. Writing and deleting single magnetic skyrmions. *Science*, 341:636–639, 2013.
- [26] M. V. Sapozhnikov, O. V. Ermolaeva, E. V. Skokhodov, N. S. Gusev, and M. N. Drozdov. Magnetic skyrmions in thickness-modulated films. *JETP Letters*, 107(6):364–368, Mar 2018.
- [27] A. F. Schäffer, Levente Rózsa, Jamal Berakdar, Elena Y. Vedmedenko, and Roland Wiesendanger. Stochastic dynamics and pattern formation of geometrically confined skyrmions. *Communications Physics*, 72:1–10, 2019.
- [28] Jan Seidel. *Topological structures in ferroic materials: domain walls, vortices and skyrmions*. Springer series in materials science. Springer, Cham, 2016.
- [29] T. H. R. Skyrme. A unified field theory of mesons and baryons. *Nuclear Physics*, 31:556–569, April 1962.
- [30] V. D. Stavrou, L. N. Gergidis, A. Markou, A. Charalambopoulos, and I. Panagiotopoulos. Micromagnetics of triangular thin film nanoelements. *Journal of Magnetism and Magnetic Materials*, 401:716–723, 2016.
- [31] Vasileios D. Stavrou, Drosos Kourounis, Konstantinos Dimakopoulos, Ioannis Panagiotopoulos, and Leonidas N. Gergidis. Magnetic skyrmions in FePt nanoparticles having reuleaux 3D geometry: a micromagnetic simulation study. *Nanoscale*, 11(42):20102–20114, 2019.
- [32] K. Tang, H.W. Zhang, Q.Y. Wen, and Z.Y. Zhong. Demagnetization field of ferromagnetic equilateral triangular prisms. *Physica B: Condensed Matter*, 363(1):96 – 101, 2005.
- [33] Arne Vansteenkiste, Jonathan Leliaert, Mykola Dvornik, Mathias Helsen, Felipe Garcia-Sanchez, and Bartel Van Waeyenberge. The design and verification of mumax3. *AIP Advances*, 4(10):107133, 2014.
- [34] X. S. Wang, H. Y. Yuan, and X. R. Wang. A theory on skyrmion size. *Communications Physics*, 1:31, 2018.
- [35] J.W. Yoo, S.J. Lee, J.H. Moon, and K.J. Lee. Phase diagram of a single skyrmion in magnetic nanowires. *IEEE Transactions on Magnetics*, 50:1500504, 2014.

- [36] Guoqiang Yu, Pramey Upadhyaya, Qiming Shao, Hao Wu, Gen Yin, Xiang Li, Congli He, Wanjun Jiang, Xiufeng Han, Pedram Khalili Amiri, et al. Room-temperature skyrmion shift device for memory application. *Nano letters*, 17(1):261–268, 2016.
- [37] Shilei Zhang, Florian Kronast, Gerrit van der Laan, and Thorsten Hesjedal. Real-space observation of skyrmionium in a ferromagnet-magnetic topological insulator heterostructure. *Nano Letters*, 18(2):1057–1063, 2018.
- [38] Shilei Zhang, Gerrit van der Laan, Jan Müller, Lukas Heinen, Markus Garst, Andreas Bauer, Helmut Berger, Christian Pfeleiderer, and Thorsten Hesjedal. Reciprocal space tomography of 3d skyrmion lattice order in a chiral magnet. *Proceedings of the National Academy of Sciences*, 115(25):6386–6391, 2018.
- [39] Xichao Zhang, Jing Xia, Yan Zhou, Daowei Wang, Xiaoxi Liu, Weisheng Zhao, and Motohiko Ezawa. Control and manipulation of a magnetic skyrmionium in nanostructures. *Phys. Rev. B*, 94:094420, Sep 2016.
- [40] Xichao Zhang, Yan Zhou, Kyung Mee Song, Tae-Eon Park, Jing Xia, Motohiko Ezawa, Xiaoxi Liu, Weisheng Zhao, Guoping Zhao, and Seonghoon Woo. Skyrmion-electronics: writing, deleting, reading and processing magnetic skyrmions toward spintronic applications. *Journal of Physics: Condensed Matter*, 32(14):143001, jan 2020.
- [41] Dapeng Zhao, Liguang Zhang, Iftikhar Ahmed Malik, Menghan Liao, Wenqiang Cui, Xinqiang Cai, Cheng Zheng, Luxin Li, Xiaopeng Hu, Ding Zhang, Jinxing Zhang, Xi Chen, Wanjun Jiang, and Qikun Xue. Observation of unconventional anomalous hall effect in epitaxial CrTe thin films. *Nano Research*, 11(6):3116–3121, Jun 2018.